A Novel Approach to Visual Navigation based on Feature Line Correspondences for Precision Landing

Wei Shao, Tianhao Gu, Yin Ma, Jincheng Xie and Liang Cao

(*College of Automation & Electronic Engineering, Qingdao University of Science and Technology, Qingdao 266042, P.R, China*)
(E-mail: gth901007@163.com)

To satisfy the needs of precise pin-point landing missions in deep space exploration, this paper proposes a method based on feature line extraction and matching to estimate the attitude and position of a lander during the descent phase. Linear equations for a lander's motion parameters are given by using at least three feature lines on the planetary surface and their two-dimensional projections. Then, by taking advantage of Singular Value Decomposition (SVD), candidate solutions are obtained. Lastly, the unique lander's attitude and position relative to the landing site are selected from the candidate solutions. Simulation results show that the proposed algorithm is able to estimate a lander's attitude and position robustly and quickly. Without an extended Kalman filter, the average errors of attitude are less than $1°$ and the average errors of position are less than $10\,\text{m}$ at an altitude of $2,000\,\text{m}$. With an extended Kalman filter, attitude errors are within $0·5°$ and position errors are within $1\,\text{m}$ at an altitude of $247·9\,\text{m}$.

1. INTRODUCTION.   The task of precise pin-point landings on other planets, moons and asteroids is always challenging and has drawn increasing recent attention. However, communication delays and low bit-rate communication between the lander and the Earth and the lack of prior information of the target planet's environments have been great challenges for deep space exploration missions (Kubota et al., 2003). Using traditional navigation methods has had limited success for precise landing, and the navigation system is required to have some autonomous functions. However, the errors of the traditional autonomous navigation method, inertial navigation, are of the order of a few kilometres as the navigation errors are always accumulating and the initial errors are hard to correct (Braun and Manning, 2007). It is hard for inertial navigation systems to meet the National Aeronautics and Space Administration (NASA) precise landing requirement that

the landing errors are less than 100 m (Qin et al., 2014; Wolf et al., 2004). In 2014, NASA tested the Lander Vision System on the new Mars Lander (Johnson and Golombek, 2012), Mars 2020 Lander Vision System Tested (2016) showed that visual navigation based on feature matching is feasible. A NASA technology report also pointed out that autonomous vision navigation in future planetary landing missions can be effective and accurate. This paper proposes a novel visual navigation technology based on feature line matching to accurately estimate a lander's attitude and position.

In 2004, the Descent Image Motion Estimation System (DIMES), the first on board optical navigation system, was designed to estimate the horizontal velocity of the *Spirit* and *Opportunity* missions by using images during the descent phase (Cheng et al., 2004). However, the stability of the matching algorithm of this system is barely satisfied, and a pair of matching points is lost in the horizontal velocity estimation process. Meanwhile, a number of optical navigation algorithms have been presented in the past 20 years. Johnson and Mathies (1999) presented an algorithm based on automatic feature tracking from a pair of descent camera images to estimate a lander's motion parameters for a small body landing. Ma and Xu (2014) proposed a real-time only feature point Light-Of-Sight (LOS) relative navigation technology utilising the theorem of triangle geometry and the filter method. The real-time nature of this algorithm can be ensured only by the on board navigation camera, and the errors of relative attitude are reduced due to the invariability of angles of unit feature point LOS vectors in this algorithm. In order to meet the pin-point landing requirement, Panahandeh and Jansson (2014) introduced the Vision-Aided Inertial Navigation (VAIN) scheme which contains a monocular camera and an Inertial Measurement Unit (IMU). It forms a novel closed-form measurement model based on the image data and IMU to overcome the shortcomings of inertial navigation systems and the attitude and position of the lander are estimated by using an Unscented Kalman Filter (UKF). More recently, algorithms based on a Stereo-Vision (SV) camera and IMU have been introduced to estimate a lander's pose respectively by two cameras or Digital Elevation Model (DEM) (Woicke and Mooij, 2018; Delaune et al., 2016). In addition, an algorithm based on crater matching was proposed to compute motion parameters by using Kronecker products (Shao et al., 2016).

Most of the algorithms mentioned above are able to meet the precise requirements of the landing, but the applications of these common navigation landmarks, feature points or craters, are clearly limited in visual navigation technologies. On the one hand, feature point extraction and matching are complex and time-consuming, and feature points can only be applied to relative navigation as the position of the feature points are not universally known. On the other hand, crater extraction and matching are difficult, and craters are sparse on some parts of the surface of planets so that the lander's motion parameters cannot be accurately estimated at sites where craters are rare.

Ridges and gullies are usually common landforms on the surface of planets, and their features are similar to lines. Thus, they can be synthesised to be feature lines as landmarks for the visual navigation. When feature lines with known position in a cartographic coordinate system are obtained from orbiters' images and are defined as the navigation landmarks, absolute navigation can be carried out and the extraction and matching of feature lines is simpler as the feature lines are easier to describe than craters. Therefore, feature lines would be a better navigation landmark and an algorithm to achieve Visual Navigation based on Feature Line Correspondences (VN-FPC) should be designed and developed. Recently, some algorithms based on line correspondences in computer vision have been proposed to

estimate pose parameters. Elqursh and Elgammal (2011) proposed an algorithm which was suitable for urban and indoor environments to estimate the pose by using the mutually parallel or orthogonal lines. Zhang et al. (2012b) presented an iterative algorithm to optimise the objective function and estimate the pose. An algorithm for perspective poses estimation from three or more line correspondences has been designed (Mirzaei and Roumeliotis., 2011). In this algorithm, the problem is transformed into non-linear least-squares, and is resolved as an eigenvalue problem using the Macaulay matrix without needing initialisation. Finally, a solution using a 16-order polynomial was presented by Zhang et al. (2012a). These algorithms have a great limitation, the range of the applications of Elqursh and Elgammal's (2011) method is small due to the use of parallel lines, and the calculation processes of the three other methods are complex and time-consuming. This paper proposes a Visual Navigation algorithm based on Feature Line Correspondences (VN-FLC) to estimate the lander's pose. By using at least three pairs of matched feature lines in a database which has been built in advance by taking advantage of data from orbiters of the target planet and their projection lines, the algorithm can easily estimate four candidate solutions of a lander's pose by using Singular Value Decomposition and select the unique lander's pose by orthogonal errors and re-projection residuals.

The remainder of this paper is organised as follows. The extraction and matching algorithms of feature lines are introduced in Section 2. Constraint equations are constructed by using the matched feature lines in a database and their extracted feature lines from landing images in Section 3. In Section 4, the lander's motion parameters are estimated, and the unique solution is determined. Then, an extended Kalman filter is constructed in Section 5. Section 6 introduces the simulation process and analyses the simulation results. Finally, the paper's conclusions are given in Section 7.

2. FEATURE LINE CORRESPONDENCES.   In order to estimate motion parameters accurately, feature lines on the plane of the planetary surface need to be extracted from their Two-Dimensional (2D) images and matched to the same feature lines with known position in the database during the descent phase. This section focuses on feature line extraction and matching algorithms.

First of all, Akinlar and Topal's (2011) extraction algorithm, EDLine (Edge Drawing Line), is applied to our proposed algorithm to extract feature lines from landing images. As this algorithm is obviously faster than more traditional algorithms, it can have a better real-time performance (Burns et al., 1986; Grompone von Gioi et al., 2008; Etemadi, 1992). As the method can directly extract the directions of feature lines and points on the feature lines, the outputs of the algorithm are consistent with the input of our visual navigation algorithm. Secondly, the algorithm presented in Zhang and Koch (2013) is selected to match the extracted feature lines from the landing image with the feature lines in a database as it takes advantage of the Line Band Descriptor (LBD), which is robust to the rotation, scaling and brightness of image to finish feature line matching. In addition, because the extracted feature lines of EDLine are fitted by using a single pixel edge from an edge drawing, it helps that the main direction of Zhang and Koch's method is found exactly. Hence, Akinlar and Topal's (2011) extraction algorithm is combined with Zhang and Koch's (2013) matching algorithm to finish feature line matching in this paper.

In this paper, the landing images taken by spacecraft *Spirit* at altitudes of approximately 1,986 m and 1,690 m and spacecraft *Curiosity* at altitudes of approximately 6,654 m and
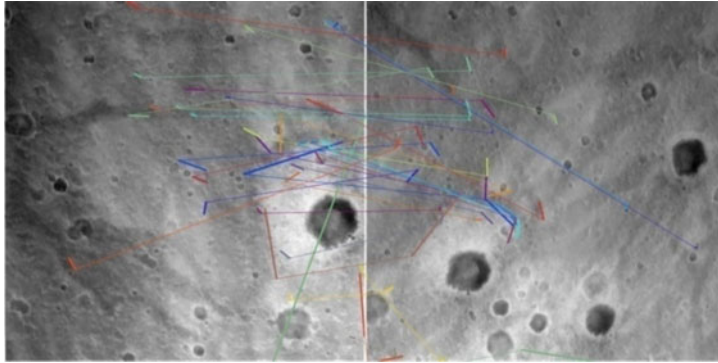
Figure 1. Feature line extraction and matching based on the images of spacecraft *Spirit*.
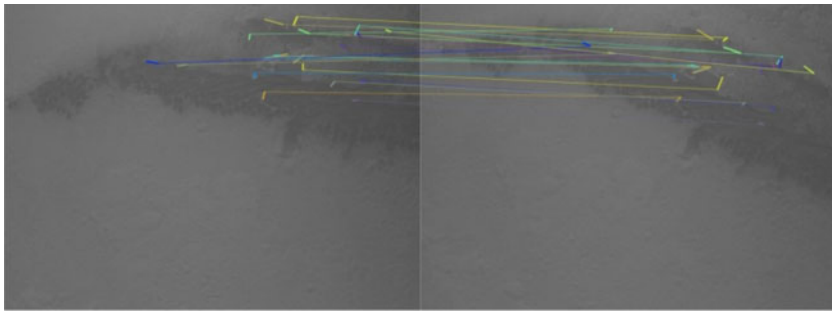

Figure 2. Feature line extraction and matching based on the images of spacecraft *Curiosity*.

6,221 m are extracted and matched by using the algorithm mentioned above (Resolution of landing images are 1024×1024 pixels). The matching results are shown in Figures 1 and 2. In the matching result of spacecraft *Spirit*, 106 and 194 feature lines from two landing images are extracted respectively in 920 ms and 1,277 ms, and 33 pairs of feature lines are matched in 97 ms. Meanwhile, the results matched by using landing images from spacecraft *Curiosity* show that 45 and 55 feature lines from two landing images are extracted respectively in 321 ms and 337 ms, and 20 pairs of feature lines are matched in 31 ms. In conclusion, because the numbers of extracted feature lines and matched feature lines are respectively more than 33 and 20, they provide a prerequisite for the development of the VN-FLC. As the time of feature line extraction and feature line matching is less than 1,277 ms and 97 ms respectively, the image processing has better real-time performance than Scale-Invariant Feature Transform (SIFT) in which the time of feature point extraction and feature line matching is more than 6 s and 3 s, respectively. (Matching conditions: CPU: Intel(R) Core(TM) i7-4558U CPU @ 2.80GHz, 4GB, Visual Studio 2013, Opencv2.4.10, ARPACK (ARnoldi PACKage), BIAS-2.8.0 (Basic Linear Algebra Subprograms), CLAPACK-3.1.1(C Language Interface of Linear Algebra PACKage), LAPACK (Linear Algebra PACKage) and SuperLU (Supernodal LU)).

3. CONSTRAINT EQUATIONS. Here, it is assumed that the planet surface is a plane and all feature lines on the planet surface are in the same plane. The coordinate systems
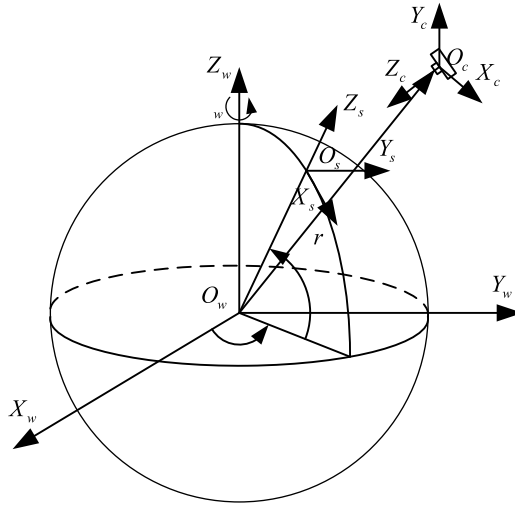
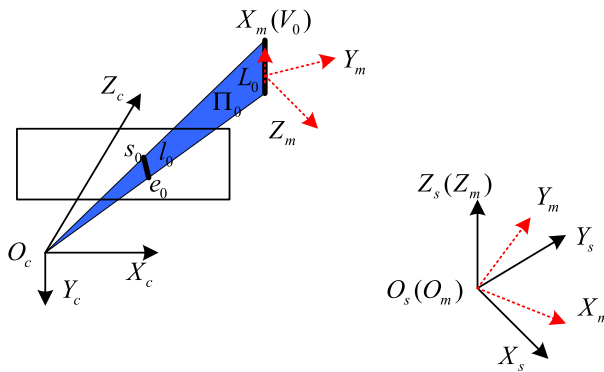Figure 3. A geometry sketch map of several common coordinate systems.

Figure 4. A geometry sketch map of model coordinate systems.

used in this paper are then introduced, and the nonlinear equations are deduced according to coordinate transformation and geometric constraints.

3.1. *Coordinate Systems.* The definition of coordinate systems is important for clearly explaining the coordinate transformation and geometric constraints. In this paper, the coordinate systems are built as Figures 3 and 4.

3.1.1. *The mass centre coordinate system* $O_w - X_w Y_w Z_w$. O_w is the mass centre of the targeted planet; $O_w X_w$ directs to the intersection between the equatorial plane and the ecliptic plane; the Z_w-axis is perpendicular to the equatorial plane; the X_w-axis, Y_w-axis and Z_w-axis meet the right-hand corkscrew rule.

3.1.2. *The cartographic coordinate system* $O_s - X_s Y_s Z_s$. O_s is the landing site; the direction of $O_s Z_s$ is the direction of vector from the mass centre of the targeted planet to the landing site; $O_s X_s$ is the vector along the tangent line of the meridian of the landing site to the south pole; X_s-axis, Y_s-axis and Z_s-axis meet the right-hand corkscrew rule.

3.1.3. *The camera coordinate system $O_c - X_c Y_c Z_c$.* O_c is the optical centre of the navigation camera; Z_c-axis is defined as the optic axis and the X_c-axis and Y_c-axis are parallel to the horizontal axis and vertical axis of image respectively.

3.1.4. *The model coordinate system $O_m - X_m Y_m Z_m$.* In this paper, $L_i = (V_i, P_i)$ denotes the 2D feature lines on the planet surface, in which V_i is defined as the unit vector of the direction of the feature lines and P_i is defined as a point on these feature lines. $l_i = (s_i, e_i)$ denotes the projection of L_i on the 2D image plane, in which s_i and e_i are defined as the endpoints of l_i. Let $O_m - X_m Y_m Z_m$ be the model coordinate system, in which V_0 is defined as the X_m-axis (the projection length of L_0 is the longest from $\{L_i\}$), the Z_m-axis is parallel to the Z_s-axis, and O_m coincides with the origin O_s of the cartographic coordinate system $O_s - X_s Y_s Z_s$.

3.2. *The perspective-3-line constraint equation.* In this paper, it is assumed that $L_i = (V_i, P_i)$ and $l_i = (s_i, e_i)$ are known. R_s^m denotes that the direction vector is rotated from the cartographic coordinate system to the model coordinate. Therefore, $V_0^m = R_s^m V_0^s = [1,0,0]^T$. It can be shown that R_s^m can be written as $[(V_0^s)^T; \varepsilon_1^T; \varepsilon_2^T]$ where ε_1 and ε_2 are mutually orthogonal and they are solutions from $(V_0^s)^T X = 0$. Similarly, the directions of the remaining feature lines are transformed from the cartographic coordinate system to the model coordinate by R_s^m, such that $V_i^m = R_s^m V_i^s$.

The plane that passes through the origin O_c of the camera coordinate system and l_i is represented as Π_i. The normal of Π_i is defined as n_i. Therefore, the rotation matrix R_m^c by which V_0^m in the cartographic coordinate system is transformed to V_0^c in the camera coordinate system must meet the constraint that $n_0^T R_m^c V_0^m = 0$. Due to this constraint, R_m^c can be decomposed as:

$$R_m^c = R R_y(\gamma) R_x(\beta)$$
$$= \begin{bmatrix} r_1 & r_2 & r_3 \\ r_4 & r_5 & r_6 \\ r_7 & r_8 & r_9 \end{bmatrix} \begin{bmatrix} \cos\gamma & 0 & -\sin\gamma \\ 0 & 1 & 0 \\ \sin\gamma & 0 & \cos\gamma \end{bmatrix} \begin{bmatrix} 1 & 0 & 0 \\ 0 & \cos\beta & -\sin\beta \\ 0 & \sin\beta & \cos\beta \end{bmatrix} \quad (1)$$

in which R is an arbitrary orthogonal identity matrix whose second column equals n_0, $R_y(\lambda)$ means a rotation whose angle around the Y-axis is equal to γ, and $R_x(\beta)$ means a rotation whose angle around the X-axis is equal to β.

R_s^c denotes that the direction vector is rotated from the cartographic coordinate system to the camera coordinate system. It is expressed as:

$$R_s^c = R_m^c R_s^m \quad (2)$$

In this condition, R_m^c can be determined by two unknown variables λ and β. Owing to the geometrical constraint that the normal n_i of the plane Π_i can be perpendicular to all lines in this plane, it meets the constraint that:

$$n_i^T R_m^c V_i^m = n_i^T R_s^c V_i^s \equiv 0 \quad (3)$$

Hence, the other two constraints can be expressed as:

$$\begin{cases} n_1 \cdot V_1^c = n_1^T R_m^c V_1^m = 0 \\ n_2 \cdot V_2^c = n_2^T R_m^c V_2^m = 0 \end{cases} \quad (4)$$

Let $\boldsymbol{n}_i^T = [x_i', y_i', z_i']$ and $\boldsymbol{V}_i^m = [a_i^m, b_j^m, 0]^T$. By substituting Equation (1) into Equation (4), the constraints can be deduced as:

$$\begin{cases} \sigma_1 \cos \gamma + \sigma_2 \sin \gamma + \sigma_3 = 0 \\ \sigma_4 \cos \gamma + \sigma_5 \sin \gamma + \sigma_6 = 0 \end{cases} \qquad (5)$$

in which

$$\begin{cases} \sigma_1 = a_1^m x_1' + b_1^m z_1' \sin \beta \\ \sigma_2 = b_1^m x_1' - a_1^m z_1' \\ \sigma_3 = b_1^m y_1' \cos \beta \\ \sigma_4 = a_2^m x_2' + b_2^m z_2' \sin \beta \\ \sigma_5 = b_2^m x_2' - a_2^m z_2' \\ \sigma_6 = b_2^m y_2' \cos \beta \end{cases}$$

By solving Equation (5), $\cos \gamma$ and $\sin \gamma$ are written as:

$$\cos \gamma = \frac{\sigma_2 \sigma_6 - \sigma_3 \sigma_5}{\sigma_1 \sigma_5 - \sigma_2 \sigma_4}, \sin \gamma = \frac{\sigma_3 \sigma_4 - \sigma_1 \sigma_6}{\sigma_1 \sigma_5 - \sigma_2 \sigma_4} \qquad (6)$$

By the geometrical constraint that $\cos^2 \gamma + \sin^2 \gamma = 1$, we can get:

$$(\sigma_2 \sigma_6 - \sigma_3 \sigma_5)^2 + (\sigma_3 \sigma_4 - \sigma_1 \sigma_6)^2 = (\sigma_1 \sigma_5 - \sigma_2 \sigma_4)^2 \qquad (7)$$

Similarly, due to $\cos^2 \beta + \sin^2 \beta = 1$, we obtain a perspective-3-line constraint equation:

$$f(r) = a_4 r^4 + a_3 r^3 + a_2 r^2 + a_1 r + a_0 = \sum_{k=0}^{4} a_k r^k = 0 \qquad (8)$$

in which r denotes $\sin \beta$.

The perspective-3-line constraint equation can be applied to estimate the four candidate solutions of $\sin \beta$, when three arbitrary feature lines on the same plane are matched with their projections.

3.3. *The Perspective-n-Line (PnL) constraint equations.*   As longer feature line projections are less affected by noise, the feature line whose projection is the second longest is selected as a guideline, and the feature line whose projection is the longest has been selected as the X_m-axis. We can construct n-2 constraint equations together with the rest of

the feature lines such as Equation (8) :

$$
\begin{cases}
f_1(r) = \sum_{k=0}^{4} a_{1k}r^4 = 0 \\[2mm]
f_2(r) = \sum_{k=0}^{4} a_{2k}r^4 = 0 \\[2mm]
\quad\vdots \\[2mm]
f_{n-2}(r) = \sum_{k=0}^{4} a_{(n-2)k}r^4 = 0
\end{cases}
\tag{9}
$$

In order to get the four candidate solutions of $\sin\beta$, the Perspective-n-Line (PnL) must be solved. However, the calculation process is difficult. Aiming at solving Equation (9) easily, an objective function is proposed in Section 4.

4. MOTION ESTIMATION. In this section, the four candidate solutions of $\sin\beta$ are solved based on the nonlinear Equation (9). Then, the four candidate solutions for the lander's pose are estimated according to the four candidate solutions of $\sin\beta$. Finally, the unique position and attitude of the lander are selected.

4.1. *Candidate solutions.* Firstly, for solving the nonlinear Equation (9), an objective function Equation (10) is constructed to pick the optimal solutions by least square methods.

$$
F = \sum_{i=1}^{n-2} f_i^{\,2}(r)
\tag{10}
$$

In order to obtain the candidate solutions, the local minima of Equation (10) is computed. Its derivative is calculated as:

$$
F' = \sum_{i=1}^{n-2} f_i(r)f_i{}'(r)
\tag{11}
$$

The minima is determined by computing the roots of its derivative Equation (11). Four roots are counted easily by the eigenvalue method and they are candidate solutions of $\sin\beta$.

Then, let P_i^s be a point on the L_i in the cartographic coordinate system and t be the coordinate of O_c in the cartographic coordinate system. Hence, we can get:

$$
n_i^T R_s^c (P_i^s - t) = 0
\tag{12}
$$

Substituting Equations (1), (2) and candidate solutions of $\sin\beta$ into Equation (4) and Equation (12), the following equation is obtained:

$$
\begin{cases}
n_i^T R R_y(\gamma) R_x(\beta_j) R_s^m V_i^s = 0 \\[2mm]
n_i^T [R R_y(\gamma) R_x(\beta_j) R_s^m P_i^s - \bar{t}] = 0
\end{cases}
\tag{13}
$$

in which $\bar{t} = R_s^c t = [x^c \quad y^c \quad z^c]^T$.

Let $n_i^T R = [\bar{x}_i, \bar{y}_i, \bar{z}_i]$, $R_x(\beta_j)R_s^m V_i^s = [a_{ij} \quad b_{ij} \quad c_{ij}]^T$ and $R_x(\beta_j)R_s^m P_i^s = [x_{ij}^m \quad y_{ij}^m \quad z_{ij}^m]^T$. A linear equation is obtained:

$$M_j Q = 0 \tag{14}$$

in which

$$M_j = \begin{bmatrix} \bar{x}_i a_{ij} + \bar{z}_i c_{ij} & \bar{z}_i a_{ij} - \bar{x}_i c_{ij} & 0 & 0 & 0 & \bar{y}_i b_{ij} \\ \bar{x}_i x_{ij}^m + \bar{z}_i z_{ij}^m & \bar{z}_i x_{ij}^m - \bar{x}_i z_{ij}^m & -x' & -y' & -z' & \bar{y}_i y_{ij}^m \end{bmatrix}$$

$$Q = \begin{bmatrix} \cos\lambda & \sin\lambda & x^c & y^c & z^c & 1 \end{bmatrix}^T$$

By solving Equation (14) with SVD, the candidate solutions of the rotation angle γ and the rotated translation vector $\bar{t}$ are obtained. Then, the candidate solution of the translation vector is calculated as $t = (R_s^c)^T \bar{t}$.

4.2. *Determination of lander's attitude and position.* The candidate solutions of R_s^c and t are calculated from the linear system Equation (14). The solutions which are affected by noise in the data extracted from images may be not a normalisation. Hence, the solutions should be normalised by a standard Three-Dimensional (3D) alignment scheme (Umeyama, 1991).

After the normalisation, the orthogonal error E_{er} of each candidate solution is computed as:

$$E_{er} = \sum_{i=1}^{n} (n_i^T R_s^c V_i)^2 \tag{15}$$

As the results of multiple experiments show that their orthogonal errors are less than 10^{-4}, the orthogonal errors of candidate solutions which are larger than 10^{-2} are deleted. The other m_1 candidate solutions are retained.

Then, P_{ni}^s is defined as the closest point on the feature line L_i to the origin of the cartographic coordinate. P_{ni}^s can be shown as:

$$P_{ni}^s = P_i^s - (P_i^s \cdot V_i^s)V_i^s \tag{16}$$

P_{ni}^c and P_i^c on the feature line L_i in the camera coordinate are obtained by using the candidate solution of the rotation matrix and the translation vector from Equation (14), and are projected onto the interpretation plane of lines $\{\bar{P}_{ni}^c\}$ and $\{\bar{P}_i^c\}$ as follows:

$$\begin{cases} P_i^c = R_s^c(P_i^s - t) \\ \bar{P}_i^c = P_i^c - (P_i^c \cdot n_i)n_i \end{cases} \tag{17}$$

$$\begin{cases} P_{ni}^c = R_s^c(P_{ni}^s - t) \\ \bar{P}_{ni}^c = P_{ni}^c - (P_{ni}^c \cdot n_i)n_i \end{cases} \tag{18}$$

Following Figure 5, we define a re-projection residual E_{re} as follows:

$$E_{re} = \int_0^{\ell_i} D_i^2(s)d(s) = \sum_{i=1}^{n} \frac{\ell_i}{3}(D_{is}^2 + D_{is}D_{ie} + D_{ie}^2) \tag{19}$$
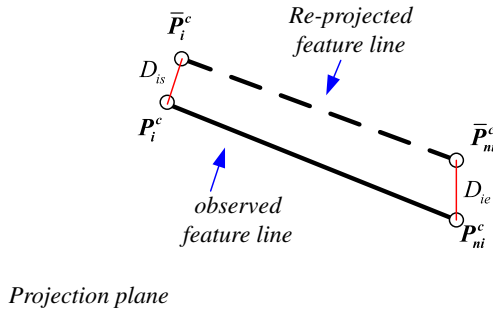
Figure 5.   Illustration of observed feature line model and re-projected feature line model on the projection plane.

in which ℓ_i is the length of the projection $\boldsymbol{l_i}$ on the image plane and D_{is} and D_{ie} denote the distance between the observed feature line endpoints and the re-projected feature line endpoints.

Substituting Equations (17) and (18) into Equation (19), we can obtain the re-projection residual E_{re} of each candidate solution and select the solution with the smallest re-projection residual as the lander's attitude and position.

Lastly, in order to improve accuracy, the lander's attitude and position are calibrated by using Kumar and Hanson's (1994) algorithm.

5.   APPLICATION OF EXTENDED KALMAN FILTER.   In this section, in order to improve the navigation accuracy, the position and attitude of the lander are estimated by an extended Kalman filter.

5.1.   *Dynamic equations.*   Following Figure 3, the dynamic model of the spacecraft's landing orbit is derived as follows. Firstly, the universal dynamic model of the lander's position in the cartographic coordinate system $O_s - X_s Y_s Z_s$ is established (Li and Cui, 2008):

$$
\begin{aligned}
\dot{\boldsymbol{r}} &= \boldsymbol{v} \\
\dot{\boldsymbol{v}} &= -2\boldsymbol{\omega_a} \times \dot{\boldsymbol{r}} + \boldsymbol{\omega_a} \times (\boldsymbol{\omega_a} \times \boldsymbol{r}) + \boldsymbol{U} + \Delta\boldsymbol{F}
\end{aligned}
\tag{20}
$$

in which $\boldsymbol{r}$ is defined as the vector from the centroid of the planet to the mass centre of the lander, $\Delta\boldsymbol{F}$ is defined as the solar radiation pressure, the third body gravity and so on, $\boldsymbol{v}$ denotes the velocity of the lander, $\boldsymbol{\omega_a}$ represents the angular velocity of the cartographic coordinate system relative to the mass centre coordinate system and $\boldsymbol{U}$ means the gravitational acceleration of the planet.

Similarly, the dynamic model of the lander's attitude at landing can be developed by the angular velocity $\boldsymbol{\omega}$ of the lander relative to the cartographic coordinate system and the angular velocity $\boldsymbol{\omega_a}$:

$$
\begin{bmatrix} \dot{\beta} \\ \dot{\gamma} \\ \dot{\alpha} \end{bmatrix} = \boldsymbol{R_b} \begin{bmatrix} \omega_x \\ \omega_y \\ \omega_z \end{bmatrix} - \boldsymbol{R_a} \begin{bmatrix} \omega_{ax} \\ \omega_{ay} \\ \omega_{az} \end{bmatrix}
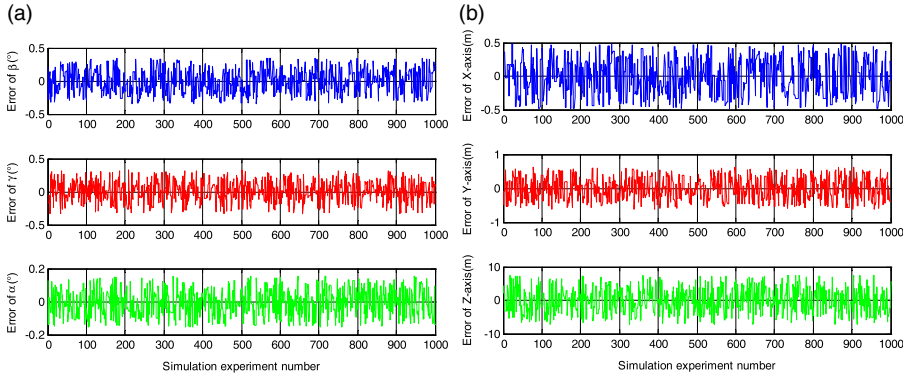\tag{21}
$$

(a)

(b)

Figure 6. Simulation without the extended Kalman filter for detecting noise: (a) lander's attitude errors; (b) lander's position errors.

in which

$$R_a = \begin{bmatrix} \dfrac{\sin\alpha}{\cos\gamma} & \dfrac{\cos\alpha}{\cos\gamma} & 0 \\ \cos\alpha & -\sin\alpha & 0 \\ \dfrac{\sin\gamma\sin\alpha}{\cos\gamma} & \dfrac{\sin\gamma\cos\alpha}{\cos\gamma} & -1 \end{bmatrix}, \quad R_b = \begin{bmatrix} 1 & \dfrac{\sin\gamma\sin\beta}{\cos\gamma} & \dfrac{\sin\gamma\cos\beta}{\cos\gamma} \\ 0 & \cos\beta & -\sin\beta \\ 0 & \dfrac{\sin\beta}{\cos\gamma} & \dfrac{\cos\beta}{\cos\gamma} \end{bmatrix}$$

5.2. *State equation.* In order to correct the attitude and position, these motion parameters are input into the state vector X:

$$X = \begin{bmatrix} x_s \\ y_s \\ z_s \\ v_x \\ v_y \\ v_z \\ \alpha \\ \beta \\ \gamma \end{bmatrix} \tag{22}$$

By taking the first derivative of X with respect to time T, the following state equation is deduced

$$\dot{X} = f(X) \tag{23}$$

in which $f(\cdot)$ is derived from the dynamic Equation (20) and Equation (21).

5.3. *Observation equation.* According to the result of 1,000 independent simulations of our algorithm without an Extended Kalman Filter (EKF), shown in Figure 6, the errors of the pose estimation of the lander can be defined as white noise whose averages are 0. The lander's parameters are shown in Table 1. The lander's motion parameters estimated

Table 1. Representative parameters of the simulation.

Parameters	Values
Lander's height	2,000 m
Noise level of 2D image's endpoints	2 pixels
Field of view	45°
Resolution	1024×1024
Focal length	14·6 mm
The number of matched feature lines	10
The surface altitude of planet	0 m

in Section 4 can be input into the observation vector Y:

$$Y = \begin{bmatrix} x_s \\ y_s \\ z_s \\ \alpha \\ \beta \\ \gamma \end{bmatrix} \qquad (24)$$

Next, a linear observation equation is obtained on the basis of the relationship between the state vector X and the observation vector Y

$$Y = H(X) \qquad (25)$$

5.4. *Extended Kalman Filter (EKF).* Here, through state Equation (23) and observation Equation (25), an EKF is created.

Firstly, the discrete state model and the discrete observation model are deduced by using Equations (23) and (25):

$$X_k = f(X_{k-1}) + w_{k-1} \qquad (26)$$

$$Y_k = H(X_k) + v_k \qquad (27)$$

where w and v respectively refer to white noise in the system and in the measurements, and

$$K = E(ww^T)$$

$$L = E(vv^T)$$

in which K and L are defined as the covariance matrix of state and the covariance matrix of observation and $E(\cdot)$ denotes the expectation.

Then, we can obtain a first order Taylor expansion of the discrete state model:

$$X_k = F_{k-1}X_{k-1} + f(\hat{X}_{k-1}) - Fk - 1\hat{X}_{k-1} + w_{k-1} \qquad (28)$$

in which Jacobi matrices are obtained by computing the first derivative of $f(X)$ with respect to X as follows:

$$F = \frac{\partial f(X)}{\partial X} \qquad (29)$$
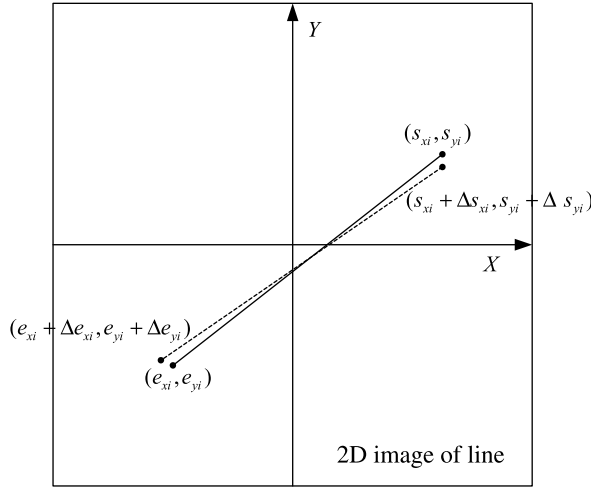
Figure 7.   The extracted errors of a feature line's 2D image.

Lastly, we can obtain the EKF:

$$\hat{X}_{k|k-1} = f(\hat{X}_{k-1}) \tag{30}$$

$$P_{k|k-1} = F_{k-1}P_{k-1}F_{k-1}^T + K_{k-1} \tag{31}$$

$$G_k = P_{k|k-1}H_k^T(H_kP_{k|k-1}H_k^T + L_k)^{-1} \tag{32}$$

$$\hat{X}_k = \hat{X}_{k|k-1} + G_k(Y_k - H(\hat{X}_{k|k-1})) \tag{33}$$

$$P_k = (I - G_kH_k)P_{k|k-1} \tag{34}$$

where $\hat{X}_0$ and P_0 are initial values of the state vector and the covariance matrix of estimation error:

$$\hat{X}_0 = E[X_0] \tag{35}$$

$$P_0 = E[(X_0 - \hat{X}_0)(X_0 - \hat{X}_0)^T] \tag{36}$$

6. SIMULATION RESULTS AND ANALYSIS. In this section, the accuracy and robustness of the proposed algorithm will be tested according to the simulation results of the lander's landing process under different conditions.

In this paper, the measurement noise of landing images is assumed to be white noise. The method for adding the measurement noise to observed feature lines on landing images is shown in Figure 7. The white noise of measurement $\{(\Delta s_i, \Delta e_i)\}$ is added to the feature line endpoints $\{(s_i, e_i)\}$ on the matched 2D projections in our simulations.

Firstly, the proposed algorithm is simulated without the EKF under different white noise intensity. The lander's attitude and position are estimated when the endpoints of observed feature lines are added to white noise intensity between 1 and 10. The rest of the simulation parameters are shown in Table 1 and the surface altitude of the planet are not considered. In this condition, we simulate the operation of our algorithm 1,000 times for each noise
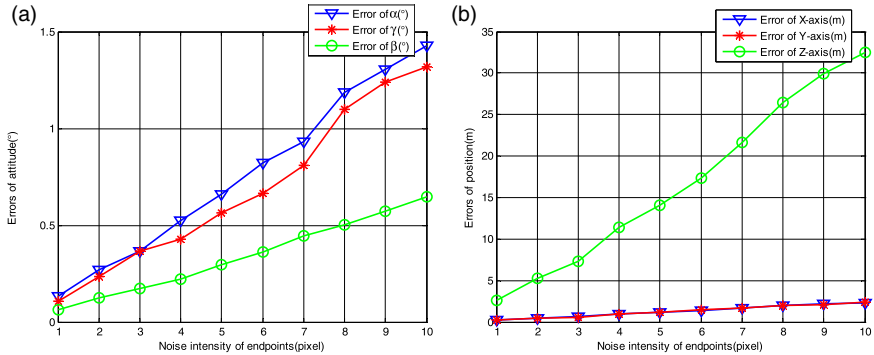
Figure 8.   Simulation without the EKF for testing the impact of noise intensity of the endpoints on accuracy:
(a) lander's attitude errors; (b) lander's position errors.

level. The motion errors along with the noise level variation are expressed in Figure 8 after eliminating gross errors by using the 3σ rule.

As shown in Figure 8, the lander's attitude errors increase along with the growth of white noise intensity, but they are less than $1\cdot5°$ as long as the noise intensity is less than 10 pixels.

The trend of the lander's position error variation is similar to the trend of attitude errors, and the error of the Z-axis which is less than 35 m within the white noise intensity from 1 to 10 pixels is more sensitive than the others which are less than 5 m. In addition, the errors of attitude and position and the corresponding measurement noise are approximately linear, and the errors are not very sensitive with the variation of the noise intensity.

The simulation without the EKF based on the variation of the number of feature lines matched with their 2D projections is discussed to testify to the accuracy and robustness of our algorithm. As the force is very weak when the number of feature lines is equal to three, gross errors in the lander's pose parameters occur easily and the lander's pose parameters can be easily affected by the white noise of feature line endpoints. By using the simulation parameters as shown in Table 1, the average errors of the lander's attitude are approximately $2\cdot5°$, and the average error of the Z-axis is equal to approximately 120 m. Hence, in order to visually display the variation of motion parameters' error along with the variation of the number of matched feature lines in the simulation figures, it is assumed that the number of matched feature lines increases from four to 14 in the 2D image taken by the on board navigation camera, and the feature line endpoints $\{(s_i, e_i)\}$ are corrupted with two pixels noise $\{(\Delta s_i, \Delta e_i)\}$. The rest of parameters of this simulation are kept as per Table 1. The motion errors under the different number of matched feature lines are shown in Figure 9 after eliminating gross errors by using the 3σ rule.

As depicted in Figure 9(a), the more the number of matched feature lines, the smaller the lander's attitude errors. When the link number of matched feature lines is more than ten, the errors begin to stabilise within $1°$. At the same time, the error of the X-axis and the error of the Y-axis are less than 1 m, and the error of the Z-axis is less than 10 m in Figure 9(b). The reasons for these are simple. With the increase of the number of matched feature lines, the constraint equation PnL contains more constraint equations, and its force becomes stronger, but when the number of feature lines reaches ten, the increase of its force is minimal. Hence, the errors are close to stable.
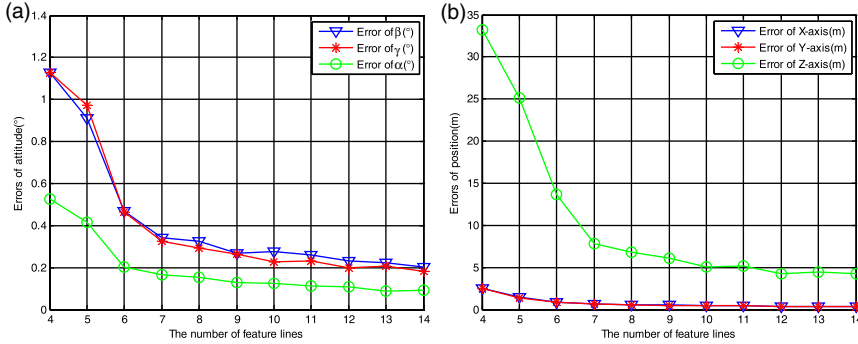
Figure 9.   The simulation without the EKF for testing the impact of the number of matched feature lines on accuracy: (a) the lander's attitude errors; (b) the lander's position errors.
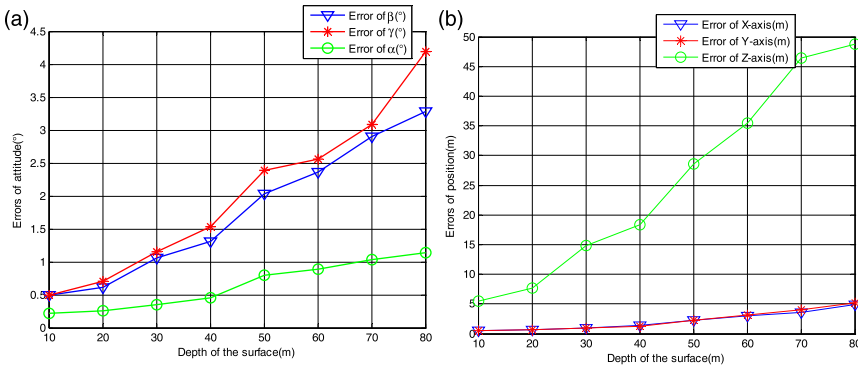

Figure 10.   The simulation without the EKF for testing the impact of the surface altitudes of planet on accuracy: (a) the lander's attitude errors; (b) the lander's position errors.

It is assumed that the visual navigation method meets the requirements of a precise landing mission when the position errors are less than 20 m and the attitude errors are less than 1·5° at an altitude of 2,000 m. The ranges of the visual navigation algorithm's applications are detected without the EKF. As the planet surface is assumed to be a plane which includes all feature lines in our algorithm, the relation between the surface altitudes of the planet and the pose errors is explored and simulated. In this simulation, we let the surface altitudes of the planet vary from 0 m to 50 m. The rest of the simulation parameters are kept as per Table 1.

The results of simulation of the surface altitudes of the planet are shown in Figure 10 after eliminating gross errors by using the 3σ rule. The errors of the lander's motion parameters are growing and the error of the Z-axis is easily affected with the increase of the surface altitudes of the planet. When the surface altitudes of the planet are larger than 40 m, the error of the Z-axis is more than 20 m and the errors of β and γ are more than 1·5°. Hence, in order to meet the requirements of a precise landing mission, the range of our visual navigation algorithm's application for the surface altitudes of the planet is 0 to 40 m at an altitude of 2,000 m.
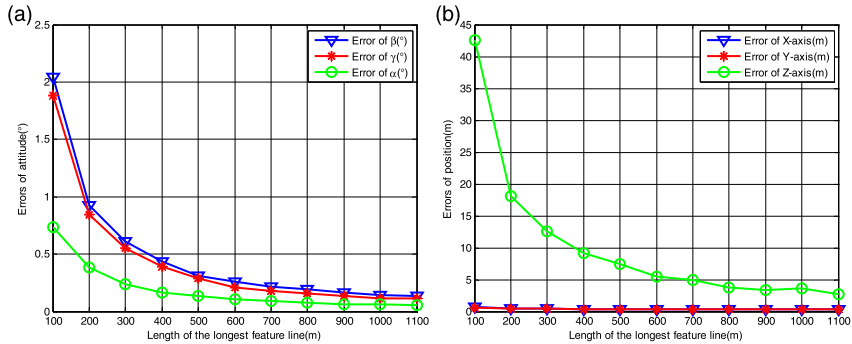
Figure 11.   The simulation without the extended Kalman filter for testing the impact of the lengths of feature lines on accuracy: (a) the lander's attitude errors; (b) the lander's position errors.

When the white noise which is added to the endpoints of the feature lines do not change, the different lengths of the feature lines have different influences on our algorithm. Hence, the range of our method's application with regard to the length of the longest feature line is considered. For this, the simulation of our visual navigation algorithm is carried out by using the parameters in Table 1 without the EKF when the length of the longest feature line varies from 100 m to 1,100 m at an altitude of 2,000 m.

In our simulation, the lander's pose errors with regard to the different lengths of the longest feature lines are displayed in Figure 11. When the length of the longest feature line becomes longer, the effects of white noise which are added to the endpoints of the longest feature line are, in theory, reduced. In this simulation, the theory is consistent with the results of the lander's pose estimation. When the length of the longest feature line is more than 200 m, the attitude errors are less than $1°$ and the position errors are less than 20 m at an altitude of 200 m. Hence, the range of our visual navigation algorithm's application with regard to the length of the longest feature line is 200 to 1,100 m due to the length of the longest feature line which can be taken at an altitude of 2,000 m being approximately 1,100 m. From Figure 1, the length of the longest feature line which is matched is more than 200 m at an altitude of 2,000 m. Therefore, our algorithm can estimate the lander's attitude and position by using landing images.

Lastly, the landing process of the NASA spacecraft *Curiosity* is simulated by using our method with the EKF (Steltzner et al., 2014). The simulation result can confirm whether the proposed algorithm meets the requirements of a pin-point landing. We hypothesise that the lander's initial height is 8·4 km above the surface after the heat shield separated and the radar-based solution converged. We assume the lander takes 103 seconds to land at an altitude of 247·9 m. The feature line endpoints $\{(s_i, e_i)\}$ are the same as for the previous simulation. The covariance matrices of the error vectors of this simulation are obtained from the white noise variances of the 1,000 repetitions of the simulation experiments at each height, and the covariance matrices of error vectors are input into the algorithm of Chang et al. (2017a; 2017b). The covariance matrices of measurement errors are obtained and applied to this simulation of the EKF. Then, the covariance matrices of the state errors are obtained from the system's white noise at each height. The rest of the parameters are kept, and the motion errors along with the landing time are illustrated in Figure 12.
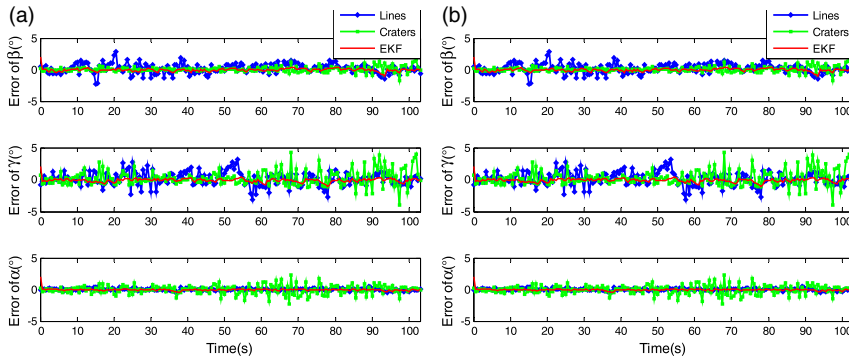
Figure 12.　The simulation for landing on Mars: (a) the lander's attitude errors; (b) the lander's position errors.

From Figure 12, the conclusion can be drawn that the result of the simulation by using the EKF is clearly better than the previous solution and the visual navigation algorithm based on crater matching of Shao et al. (2016). After the extended Kalman filtering, the lander's attitude errors are stable within 0·5° and the lander's position errors decrease with decreasing altitude to within 1 m at a height of about 247·9 m. This is because 2D images become sharper with the decreasing altitude of the lander. Hence the effect of noise is smaller.

In summary, all simulation of our proposed algorithm proves that the new algorithm can estimate the lander's pose parameters during the descent phase.

7. CONCLUSIONS.　A novel algorithm is presented to estimate a lander's attitude and position in this paper. The proposed algorithm can obtain a unique solution of a lander's motion parameters by using at least three feature lines with known position on the surface of a targeted planet in a database of their projection lines. The accuracy and robustness of our algorithm are demonstrated by a series of simulations. The lander's attitude errors are less than 0·5° and the lander's position errors are less than 1 m. However, the method is limited, because the position of the feature lines must be known in advance in a database. Hence, in future study, the relative attitude and position of the lander will be estimated by using the feature lines from sequence images during the descending phase when the absolute positions of feature lines are unknown.

REFERENCES

Akinlar, C. and Topal, C. (2011). EDLines: A real-time line segment detector with a false detection control. *Pattern Recognition Letters*, **32**(13), 1633–1642.

Braun, R. D. and Manning, R. M. (2007). Mars exploration entry, descent, and landing challenges. *Journal of Spacecraft and Rockets*, **44**(2), 310–323.

Burns, J. B., Hanson, A. R. and Riseman, E. M. (1986). Extracting straight lines. *IEEE Transactions on Pattern Analysis and Machine Intelligence*, **PAMI-8**(4), 425–455.

Chang, G., Xu, T. and Wang, Q. (2017a). Error analysis of the 3D similarity coordinate transformation. *GPS Solutions*, **21**(3), 963–971.

Chang, G., Xu, T., Wang, Q. and Liu, M. (2017b). Analytical solution to and error analysis of the quaternion-based similarity transformation considering measurement errors in both frames. *Measurement*, **110**, 1–10.

Cheng, Y., Goguen, J., Johnson, A., Leger, C., Matthies, L., Martin, M. S. and Willson, R. (2004). The Mars exploration rovers descent image motion estimation system. *IEEE Intelligent Systems*, **19**(3), 13–21.

Delaune, J., Le Besnerais, G., Voirin, T., Farges, J. L. and Bourdarias, C. (2016). Visual–inertial navigation for pinpoint planetary landing using scale-based landmark matching. *Robotics and Autonomous Systems*, **78**, 63–82.

Elqursh, A. and Elgammal, A. (2011). Line-based relative pose estimation. *In Computer Vision and Pattern Recognition (CVPR), 2011 IEEE Conference*, 3049–3056.

Etemadi, A. (1992). Robust segmentation of edge data. In *Image Processing and its Applications, 1992 International Conference on.* IET, 311–314.

Grompone von Gioi, R., Jakubowicz, J., Morel, J. M. and Randall, G. (2008). On straight line segment detection. *Journal of Mathematical Imaging and Vision*, **32**(3), 313–347.

Grompone von Gioi, R., Jakubowicz, J., Morel, J. M. and Randall, G. (2010). LSD: A fast line segment detector with a false detection control. *IEEE Transactions on Pattern Analysis and Machine Intelligence*, **32**(4), 722–732.

Johnson, E. A. and Mathies, H. L. (1999). Precise image-based motion estimation for autonomous small body exploration. *Artificial Intelligence, Robotics and Automation in Space*, **440**, 627–634.

Johnson, A. E. and Golombek, M. P. (2012). Lander vision system for safe and precise entry descent and landing. *In Concepts and Approaches for Mars Exploration*, **1679**, 12–14

Kubota, T., Hashimoto, T., Sawai, S., Kawaguchi, J. I., Ninomiya, K., Uo, M. and Baba, K. (2003). An autonomous navigation and guidance system for MUSES-C asteroid landing. *Acta Astronautica*, **52**(2), 125–131.

Kumar, R. and Hanson, A. R. (1994). Robust methods for estimating pose and a sensitivity analysis. *CVGIP: Image Understanding*, **60**(3), 313–342.

Li, S. and Cui, P. (2008). Landmark tracking based autonomous navigation schemes for landing spacecraft on asteroids. *Acta Astronautica*, **62**(6), 391–403.

Ma, H. and Xu, S. (2014). Only feature point line-of-sight relative navigation in asteroid exploration descent stage. *Aerospace Science and Technology*, **39**, 628–638.

Mars 2020 Lander Vision System Tested. (2016). http://mars.nasa.gov/news/mars-2020-lander-vision-system-tested&s=6.

Mirzaei, F. M. and Roumeliotis, S. I. (2011). Globally optimal pose estimation from line correspondences. *InRobotics and Automation (ICRA), 2011 IEEE International Conference*, 5581–5588.

Panahandeh, G. and Jansson, M. (2014). Vision-aided inertial navigation based on ground plane feature detection. *IEEE/ASME Transactions on Mechatronics*, **19**(4), 1206–1215.

Qin, T., Zhu, S., Cui, P. and Gao, A. (2014). An innovative navigation scheme of powered descent phase for Mars pinpoint landing. *Advances in Space Research*, **54**(9), 1888–1900.

Shao, W., Gao, X., Xi, S., Leng, J. and Gu, T. (2016). Attitude and position determination based on craters for precision landing. *Proceedings of the Institution of Mechanical Engineers, Part G: Journal of Aerospace Engineering*, **230**(10), 1934–1942.

Steltzner, A. D., Miguel San Martin, A., Rivellini, T. P., Chen, A. and Kipp, D. (2014). Mars Science Laboratory Entry, Descent, and Landing System Development Challenges. *Journal of Spacecraft and Rockets*, **51**(4), 994–1003.

Umeyama, S. (1991). Least-squares estimation of transformation parameters between two point patterns. *IEEE Transactions on Pattern Analysis and Machine Intelligence*, **13**(4), 376–380.

Woicke, S. and Mooij, E. (2018). Terrain Relative Navigation for Planetary Landing Using Stereo Vision Measurements Obtained from Hazard Mapping. *In Advances in Aerospace Guidance, Navigation and Control*, Springer, Cham, 731–751.

Wolf, A. A., Graves, C., Powell, R. and Johnson, W. (2004). Systems for pinpoint landing at Mars. *In 14th AIAA/AAS Space Flight Mechanics Meeting*.

Zhang, L., Xu, C., Lee, K. M. and Koch, R. (2012a). Robust and efficient pose estimation from line correspondences. *In Asian Conference on Computer Vision*, 217–230.

Zhang, L. and Koch, R. (2013). An efficient and robust line segment matching approach based on LBD descriptor and pairwise geometric consistency. *Journal of Visual Communication and Image Representation*, **24**(7), 794–805.

Zhang, X., Zhang, Z., Li, Y., Zhu, X., Yu, Q. and Ou, J. (2012b). Robust camera pose estimation from unknown or known line correspondences. *Applied Optics*, **51**(7), 936–948.